

## UC Merced

### UC Merced Previously Published Works

**Title**

Barriers to front propagation in laminar, three-dimensional fluid flows

**Permalink**

<https://escholarship.org/uc/item/3b15240w>

**Journal**

Physical Review E, 97(3)

**ISSN**

2470-0045

**Authors**

Doan, Minh  
Simons, JJ  
Lilienthal, Katherine  
[et al.](#)

**Publication Date**

2018-03-01

**DOI**

10.1103/physreve.97.033111

Peer reviewed

# Barriers to front propagation in laminar, three-dimensional fluid flows

Minh Doan,<sup>1,\*</sup> JJ Simons,<sup>1</sup> Katherine Lilienthal,<sup>1</sup> Kevin Mitchell,<sup>2,†</sup> and Tom Solomon<sup>1,‡</sup>

<sup>1</sup>*Department of Physics and Astronomy, Bucknell University, Lewisburg, PA 17837, USA*

<sup>2</sup>*School of Natural Sciences, University of California, Merced, CA 95344, USA*

(Dated: July 28, 2017)

We present the first experiments on one-way barriers that block reaction fronts in a fully three-dimensional (3D) fluid flow. Fluorescent Belousov-Zhabotinsky reaction fronts are imaged with laser-scanning in a laminar, overlapping vortex flow. The barriers are analyzed with a 3D extension to burning invariant manifold (BIM) theory that was previously applied to 2D advection-reaction-diffusion processes. We discover tube and sheet barriers that guide the front evolution. The experimentally-determined barriers are explained by BIMs calculated from a model of the flow.

PACS numbers: 82.40.Ck, 47.52.+j, 47.10.Fg, 47.70.Fw

Numerous chemical, biological, atmospheric and oceanic processes are characterized by the propagation of a front that separates two different phases. In many of these processes, the front propagation is strongly affected by fluid flows in the system. This generalized advection-reaction-diffusion (ARD) problem [1, 2] has applications in a wide variety of systems, including microfluidic chemical and biological devices [3, 4]; cellular- and embryonic-scale biological processes [5]; oceanic-scale algal blooms [6, 7]; the ignition stages of a supernova explosion [8]; and the propagation of a disease in a mobile society [9]. Previous experiments [10–13] have identified dynamically-defined, one-way barriers that block reaction fronts propagating in a wide range of two-dimensional (2D), laminar flows. These barriers have been explained theoretically [10, 14–17] as *burning invariant manifolds* (BIMs) that are generalizations of passive invariant manifolds [18–22] that impede passive mixing in a flow. But most ARD processes involve flows that are three-dimensional (3D). The question of whether BIMs can be generalized to 3D flows is important toward developing a comprehensive theory of front propagation in ARD systems.

In this Letter, we present the first experimental study of front propagation in a laminar, 3D fluid flow, along with an extension of the BIM theory to account for the additional spatial dimension. The extension from 2D to 3D is accompanied by several topological questions: (1) Are there generalized BIMs that also act as barriers that impede the motion of reaction fronts for 3D flows? (2) What is the topology of these barriers – if they exist – for a 3D flow? (3) Are the barriers one-way, similar to their 2D counterparts? (4) How does the structure of these barriers depend on the flow and reaction-diffusion front speeds?

The flow is a superposition of horizontal and vertical chains of vortices, generated experimentally using a magnetohydrodynamic technique (Fig. 1). An electrical current passes lengthwise through fluid in an optical-quality quartz cell. The current interacts with a magnetic field produced by two chains of five 3/4" Nd-Fe-B magnets, one below and the other behind the cell. The magnets

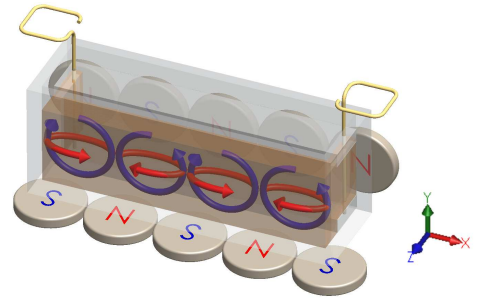


FIG. 1: (Color online) Fluid cell, showing the magnetohydrodynamic forcing and the resulting flow formed from the superposition of a horizontal (red) and vertical (blue) chain of vortices. The fluid channel measures 0.80 cm x 8.0 cm horizontally with a height of 1.9 cm.

below the cell produce the horizontal vortex chain and the magnets behind produce the vertical vortices. The bottom and side magnets are aligned so that the superposed vortex chains line up.

The fluid in the cell is composed of the chemicals used for the excitable Ruthenium (Ru)-catalyzed Belousov-Zhabotinsky (BZ) chemical reaction [23–25]. The Ru indicator is initially in its orange, reduced state, but when triggered (either naturally or manually by inserting a silver wire), the indicator is oxidized, producing a green, pulse-like, autocatalytic reaction front that propagates with a speed  $V_0 = 70 \mu\text{m}/\text{s}$  in the absence of a flow. The electrical current and imposed electrical field ( $< 0.1 \text{ V}/\text{cm}$ ) are small enough to avoid significant effects on the front propagation speed [26]. Measurements of front speeds without an electrical current also indicate a negligible effect from the permanent magnets [27]. We also neglect curvature effects on front speeds [1].

Three-dimensional BZ patterns have been imaged previously [28], but only for stagnant systems. These are the first experiments to obtain full 3D imaging of the time-evolution of BZ reaction fronts in a fluid flow. We use a scanning, laser-induced fluorescence technique that takes advantage of the fact that the Ru indicator flu-

oresces when reduced but not when oxidized. A 400-mW, 405 nm laser beam is reflected off a pair of voltage-controlled mirrors. One mirror oscillates rapidly, causing the beam to scan horizontally through the cell; the other mirror scans through 50 different heights in the cell. For each height, the fluorescence of the reduced Ru is imaged from above with an sCMOS video camera. The result is a stack of 50 images which can be reconstructed into a full 3D view of the evolving reaction front.

Particle image velocimetry (PIV) is used to characterize the flow. We model the flow as the superposition of two vortex chains described by streamfunctions

$$\begin{aligned}\psi_1(x, y, z) &= -\frac{1}{\pi} \cos(\pi x)W(y)f(z), \\ \psi_2(x, y, z) &= -\frac{1}{\pi} \cos(\pi x)W(z)g(y).\end{aligned}\quad (1)$$

The velocity field is derived from these streamfunctions via  $u_x(x, y, z) = \partial\psi_1/\partial y + \partial\psi_2/\partial z$ ,  $u_y(x, y, z) = -\partial\psi_1/\partial x$ , and  $u_z(x, y, z) = -\partial\psi_2/\partial x$ . In Eq. (1),  $f(z) = 0.5(1 + 0.5[1 + \cos(2\pi z)])$  and  $g(y) = a(y + 0.5) \exp[-b(y + 0.5)] + c$  (with  $a=46$ ,  $b=7.8$  and  $c=0.9$ ) are taper functions (fitted to the PIV data) to account for variation of the vortex strengths with distance from the magnets. The function  $W$  [29] depends on the boundary conditions at the side and top/bottom surfaces. In the simplest case with free-slip boundary conditions,

$$W(y) = \cos(\pi y). \quad (2)$$

In this paper, we use more realistic no-slip boundary conditions [29], with

$$\begin{aligned}W(y) &= \cos(q_0 y) - A_1 \cosh(q_1 y) \cos(q_2 y) + \\ &A_2 \sinh(q_1 y) \sin(q_2 y),\end{aligned}\quad (3)$$

with  $q_0 = 3.973638032476331$ ,  $q_1 = 5.194998480822572$ ,  $q_2 = 2.125929469473915$ ,  $A_1 = 0.061508353836287$ , and  $A_2 = 0.103869826106854$ . In Eq. (1), the  $xyz$ -coordinates are non-dimensionalized by the vortex length, height, and width, so that a single vortex occupies a unit cell. Similarly, the resulting fluid velocities are non-dimensionalized by the maximum velocity of the second vortex chain.

We define a dimensionless front propagation speed  $v_0 \equiv V_0/U$ , where  $U$  is the maximum (dimensionful) fluid velocity of the second vortex chain. Note that there is no advective (passive) transport between adjacent vortices in this flow.

Examples of evolving reaction fronts are shown in Fig. 2. Two of the most dominant barriers are shown in these sequences: a quarter-tube barrier that follows an edge of the unit cell and forms an arch that spans two neighboring vortices (Fig. 2a) and a large sheet-like barrier that forms near the boundary between neighboring vortices (Fig. 2b). Reactions propagating in a particular direction do not penetrate through these barriers

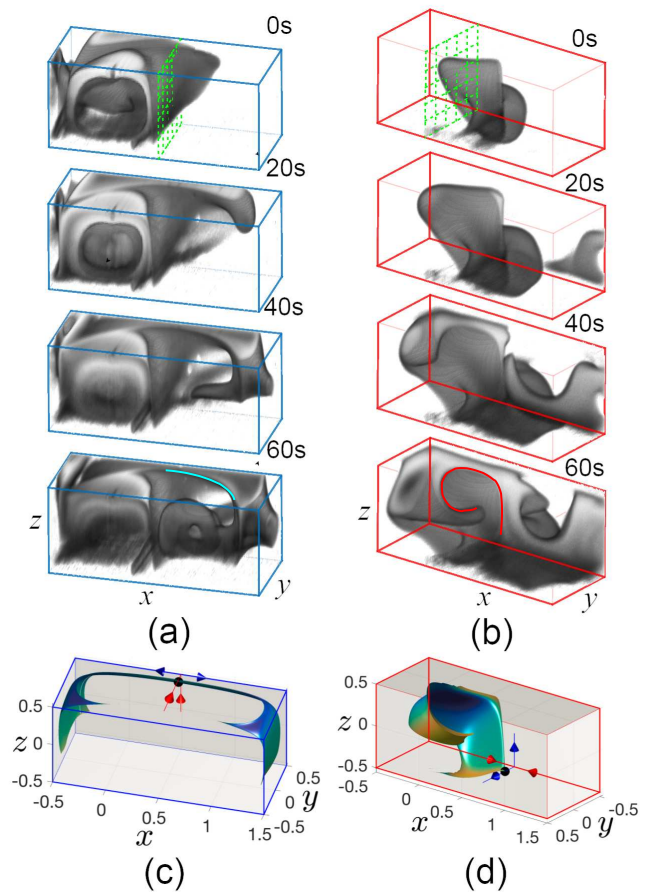


FIG. 2: (Color online) Sequences showing the evolution of reaction fronts for the middle two unit cells (4.0 cm) of the overlapping vortex flow. (a)  $v_0 = 0.064$ ; the evolving front (viewed at an angle from above) is blocked by a quarter-tube, arch-like barrier that spans two vortices. The leading edge of this barrier is shown as a cyan curve in the 60 s image. (b)  $v_0 = 0.16$ ; the evolving front (viewed at an angle from below) is blocked by a scroll-shaped, sheet barrier, the edge of which is shown in red in the 60 s image. Movie versions of these sequences can be found online in Supplementary Material. (c) and (d) Simulated burning invariant manifolds corresponding to the barriers seen in (a) and (b). The dots show the burning fixed points to which the BIMs are attached. The red (blue) arrows show the stable (unstable) directions of the fluid flow near the advective fixed point.

but must circumnavigate them, similar to reaction barriers observed in previous 2D experiments. Note that the sheet-like barrier (Fig. 2b) wraps into the left vortex. A reaction front going to the left passes the advective separatrix between the vortices, hits the vertical part of this barrier and wraps around over the top of the vortex. The front penetrates into the center of the left vortex only because the barrier itself scrolls into the center.

Convergence of the experimental reaction fronts and the one-way nature of these barriers can be seen in Figs. 3 and 4. Column (b) of both of these figures shows fronts

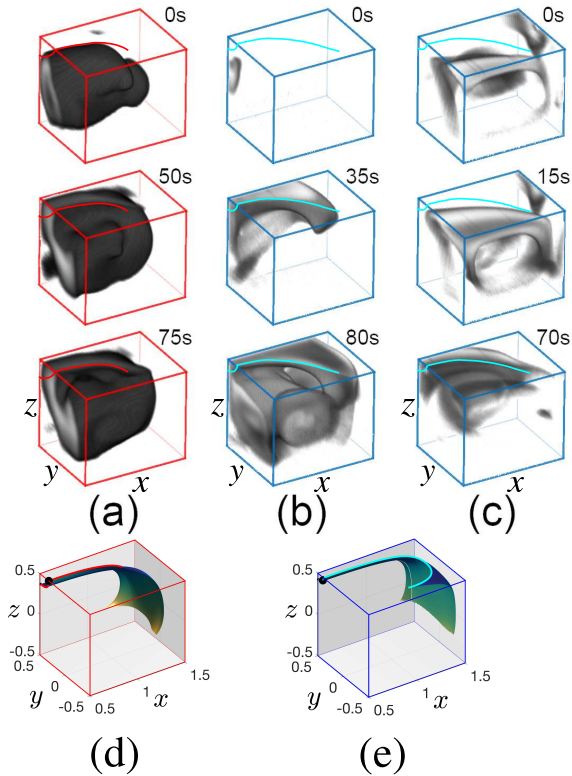


FIG. 3: (Color online) Part of the quarter-tube, arch-like barrier. (a)  $v_0 = 0.16$ ; (b) and (c)  $v_0 = 0.064$ . The front left surface corresponds to the green grid in Fig. 2(a). In (a) and (b), the front enters the quarter-tube from the back and is blocked by the tube-barrier as it moves in the  $-y$  direction near the top surface. In (c), a front moving in the  $+y$  direction near the top penetrates into the quarter-tube. Panels (d) and (e) show numerically computed BIMs corresponding to the same viewing region and  $v_0$  as columns a and b/c.

converging on – but not passing through – part of a BIM, while column (c) shows fronts penetrating through the BIMs in the opposite direction.

The locations of these barriers also depend on the non-dimensional front propagation speed  $v_0$ , also shown in Figs. 3 and 4. The barriers are farther away from the vortex boundaries (where passive invariant manifolds reside) for larger  $v_0$  (denoted by red boxes in each figure).

The topology of the barriers can be qualitatively understood by considering the Eulerian fixed points of the simple free-slip flow given by Eq. (1) with  $W$  in Eq. (2). The eight corners of each vortex cell are hyperbolic fixed points with either two stable and one unstable directions (SSU) or one stable and two unstable directions (SUU). If triggered near an SSU fixed point (Fig. 5a), a reaction front will flow outward with the unstable direction; it will also propagate outward *against* the two stable directions, until balanced by the incoming flow, where  $|\mathbf{u}| = v_0$ . The result is a tube-like, one-way barrier (Fig. 5a) that confines reactions propagating outward, but allows reactions

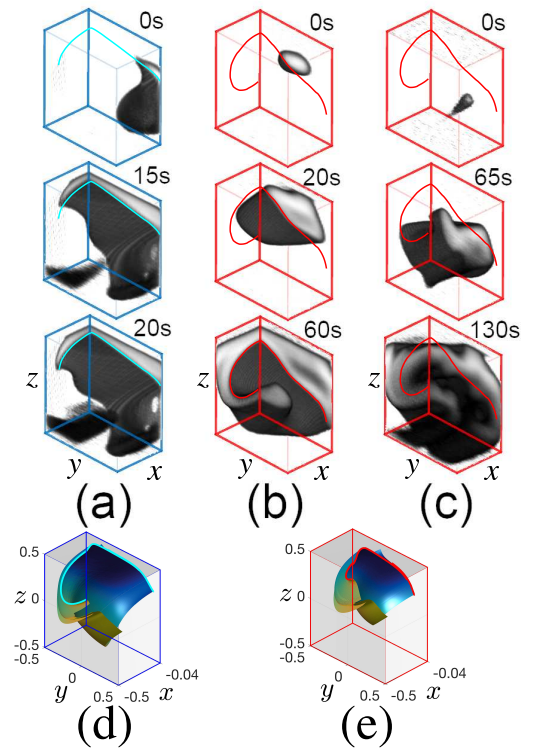


FIG. 4: (Color online) Part of the sheet (scroll) barrier. (a)  $v_0 = 0.064$ ; (b) and (c)  $v_0 = 0.16$ . The front right surface corresponds to the green grid in Fig. 2(b). In (a) and (b), a front above the barrier (partially drawn in cyan and red curves) is blocked from propagating downward by the barrier. In (c), a front propagating upward passes through the (one-way) barrier. Panels (d) and (e) show numerically computed BIMs corresponding to the same viewing region and  $v_0$  as columns a and b/c. Compared to Fig. 2 (d), part of a second BIM has also been plotted near  $y = -0.5$ .

propagating inward to penetrate the tube.

If triggered near an SUU fixed point (Fig. 5b), the reaction will flow outward along the two unstable directions and will also propagate outward against the single stable direction until balanced by the incoming flow, where  $|\mathbf{u}| = v_0$ . The result is two one-way sheet barriers (Fig. 5b), each of which blocks reactions going away from the SUU fixed point.

To quantitatively analyze the behavior of reaction fronts in a 3D flow, we extend the previous 2D BIM theory [10–17], in which we directly model the motion of an infinitesimal element of the reaction front. In 2D, a front element is parameterized by two spatial coordinates and a single orientation angle. In 3D, a minimal model requires three spatial dimensions and two orientation angles. However, it is computationally easier to characterize the orientation of a front element using the three  $xyz$ -components of its unit normal vector  $\mathbf{n}$ . The result is a 6D set of ODEs (with the 5D system embedded

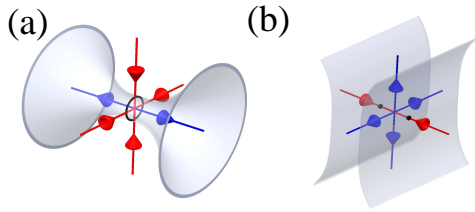


FIG. 5: (Color online) (a) Cartoon of a tube-like reaction barrier expected near an advective fixed point with SSU stability and equal stable flow rates. (b) Cartoon of sheet-like reaction barriers expected near an SUU fixed point.

as the invariant subspace  $|\mathbf{n}| = 1$ ):

$$\begin{aligned} \frac{dr_i}{dt} &= u_i + v_0 n_i, \\ \frac{dn_i}{dt} &= n_i \sum_{j,k} u_{j,k} n_j n_k - \sum_j u_{j,i} n_j, \quad i, j, k = x, y, z, \end{aligned} \quad (4)$$

where  $u_i$  and  $n_i$  are the components of the fluid velocity field and unit normal, respectively, and  $u_{j,k}$  is the partial derivative of  $u_j$  in the  $k$  direction. The first equation denotes motion of the front element due to advection (first term) and burning, i.e., propagation of the front relative to the fluid in the normal direction (second term). The second equation denotes rotation of the front element due to the flow.

A *burning fixed point* is a position  $\mathbf{r}$  and orientation  $\mathbf{n}$  where  $d\mathbf{r}/dt = d\mathbf{n}/dt = 0$  in Eq. (4). According to the prior Fig. 5 discussion, these often occur near advective fixed points, with two burning fixed points near an SUU point and a circle of fixed points near an SSU point (with equal unstable flow rates). See the black dots in Fig. 5. The BIMs are calculated by integrating trajectories of Eq. (4) away from the burning fixed points.

For comparison to the experiments, we use no-slip boundary conditions, Eq. (3). Though the number and positions of the burning fixed points are more complicated than for Eq. (2), the same computational approach generates the BIMs; see Figs. 2c and 2d. The BIM in Fig. 2c is a quarter tube that flairs out away from the burning fixed point (black dot), forming an arch that mimics the experimental barrier in Fig. 2a. It also matches one quarter of the cartoon in Fig. 5a, since the BIM in Fig. 2c surrounds an SSU advective fixed point on the edge of the domain. The quarter-tube geometry is especially clear in the cross-section Fig. 3e, which corresponds to the experiments in Figs. 3b and 3c. Similarly, Fig. 3d shows the BIM cross-section for the larger  $v_0$  value, corresponding to Fig. 3a. Note that the larger  $v_0$  produces a fatter tube, as in the experiments. Though the tube BIM only blocks reactions propagating outward, it can still act as a trip-wire for reactions initiated outside the tube. A front that encounters a tube BIM penetrates inside but then is trapped by the outward-blocking nature of the BIM; see Fig. 3b, in which a reaction triggered

below the back of the tube penetrates into the BIM but is stopped by the outward-blocking BIM as the front moves in the  $-y$  direction near the top.

Comparing the numerical BIM in Fig. 2d to the experiment in Fig. 2b, they both exhibit the same scroll behavior. Near the boundary between the two vortices, Fig. 2d also resembles the cartoon in Fig. 5b, having a flat sheet-like surface normal to the fluid inflow direction  $\hat{\mathbf{x}}$ . Figures 4d and 4e show cross-sections of the scroll BIM for the two  $v_0$  values, comparable to the experiments in Figs. 4a and 4b/c. Each theory figure actually shows two BIMs, so close together they appear as one: the original BIM from Fig. 2 and a second BIM in the gap between the original BIM and the front left surface. As seen by the red and cyan intersection curves, these BIMs show the same scroll structure as the experiments, including the fact that the larger  $v_0$  value creates a BIM closer to the vortex center. For both the tube and scroll, the experimental and theoretical BIMs differ in their detailed structure. But this is to be expected given the simple analytical form of the fluid velocity field Eq. (1).

There are more BIMs in this system than observed in these experiments. For example, symmetry dictates that the BIM in Fig. 2d reflects about the midplane to a second BIM on the right. However, this BIM is not seen in Fig. 2b because the reaction fronts pass through it in the allowed direction.

In summary, we experimentally visualized one-way barriers that block the motion of reaction fronts in a truly 3D laboratory-scale fluid flow. We developed a 3D extension of the burning invariant manifold theory, used previously only in 2D, which provides a theoretical explanation and framework for studying these reaction barriers. Using an explicit form of the flow field, direct numerical computation shows that the shape of the BIMs captures the essential geometry of the experimentally measured barriers. This theory applies to much more than chemical reactions; given any flow and any process that produces a sharp propagation front (with zero-flow propagation speed  $V_0$ ), the BIMs predicted by Eq. (4) will identify one-way barriers that impede the motion of that front. Ultimately, the success of the BIM approach for identifying reaction front barriers in both 2D and now 3D flows suggests that this approach could form the basis for a more comprehensive theory of front propagation in fluid flows.

These studies were supported by the US National Science Foundation under grants DMR-1361881, DUE-1317446, PHY-0748828, and CMMI-1201236. We would like to thank Jack Raup, Moises Veloz and Joe Tolman for assistance with the milling of the apparatus. KAM would like to thank Marcos Mendoza for initial discussions on the 3D theory of BIMs.

- 
- \* current address: Department of Mechanical Engineering, Keio University, 3-14-1 Hiyoshi, Kohoku-ku, Yokohama, Kanagawa, 223-8522, Japan. Email: mndoan@keio.jp
- † Electronic address: [kmitchell@ucmerced.edu](mailto:kmitchell@ucmerced.edu)
- ‡ Electronic address: [tsolomon@bucknell.edu](mailto:tsolomon@bucknell.edu)
- [1] Z. Neufeld and E. Hernandez-Garcia, *Chemical and Biological Processes in Fluid Flows: A Dynamical Systems Approach* (Imperial College Press, 2009).
- [2] A. Tzella and J. Vanneste, *Phys. Rev. E* **90**, 011001(R) (2014).
- [3] T. John and I. Mezic, *Phys. Fluids* **19** (2007).
- [4] C. L. A. Berli and P. A. Kler, *Microfluid Nanofluid* **20**, 104 (2016).
- [5] P. K. Trong, J. Guck, and R. E. Goldstein, *Phys. Rev. Lett.* **109**, 028104 (2012).
- [6] E. Hernandez-Garcia and C. Lopez, *Ecol. Complexity* **1**, 253 (2004).
- [7] D. Bastine and U. Feudel, *Nonlinear Processes in Geophysics* **17**, 715 (2010).
- [8] C. M. Malone, A. Nonaka, S. E. Woosley, A. S. Almgren, J. B. Bell, S. Dong, and M. Zingale, *Astro. J.* **782**, 1 (2014).
- [9] J. Ge, K. I. Kim, Z. Lin, and H. Zhu, *J. Differential Equations* **259**, 5486 (2015).
- [10] J. Mahoney, D. Bargteil, M. Kingsbury, K. Mitchell, and T. Solomon, *Europhys. Lett.* **98**, 44005 (2012).
- [11] D. Bargteil and T. Solomon, *Chaos* **22**, 094107 (2012).
- [12] P. W. Megson, M. L. Najarian, K. E. Lilienthal, and T. H. Solomon, *Phys. Fluids* **27**, 023601 (2015).
- [13] S. Gowen and T. Solomon, *Chaos* **25**, 087403 (2015).
- [14] K. A. Mitchell and J. R. Mahoney, *Chaos* **22**, 037104 (2012).
- [15] J. R. Mahoney and K. A. Mitchell, *Chaos* **23**, 043106 (2013).
- [16] J. R. Mahoney and K. A. Mitchell, *Chaos* **25**, 087404 (2015).
- [17] J. R. Mahoney, J. Li, C. Boyer, T. Solomon, and K. A. Mitchell, *Phys. Rev. E* **92**, 063005 (2015).
- [18] R. S. MacKay, J. D. Meiss, and I. C. Percival, *Physica D* **13**, 55 (1984).
- [19] V. Rom-Kedar, *Nonlinearity* **7**, 441 (1994).
- [20] T. H. Solomon, S. Tomas, and J. L. Warner, *Phys. Rev. Lett.* **77**, 2682 (1996).
- [21] G. Haller, *Physics of Fluids* **13**, 3365 (2001).
- [22] G. A. Voth, G. Haller, and J. P. Gollub, *Phys. Rev. Lett.* **88**, 254501 (2002).
- [23] S. K. Scott, *Oscillations, Waves, and Chaos in Chemical Kinetics* (Oxford University Press, Oxford, 1994).
- [24] R. Kapral and E. K. Showalter, *Chemical Waves and Patterns* (Kluwer, Dordrecht, Netherlands, 1995).
- [25] Initial concentrations of the reactants for each run are:  $[\text{BrMA}] = 0.09 \text{ M}$ ,  $[\text{MA}] = 0.03 \text{ M}$ ,  $[\text{BrO}_3^-] = 0.16 \text{ M}$ ,  $[\text{H}_2\text{SO}_4] = 0.25 \text{ M}$ ,  $[(\text{Ru}(\text{bpy})_3)^{2+}] = 0.3 \text{ mM}$ .
- [26] M. Pornprompanya, S. C. Muller, and H. Seveikova, *Phys. Chem. Chem. Phys.* **4**, 3370 (2002).
- [27] H. Okano and H. Kitahata, *Bioelectromagnetics* **34**, 220 (2013).
- [28] J. Tamás Bánsági and O. Steinbock, *Chaos* **18**, 026102 (2008).
- [29] S. Chandrasekhar, *Hydrodynamic and Hydromagnetic Stability* (Clarendon, Oxford, 1961).